nature communications

Article

https://doi.org/10.1038/s41467-024-53893-z

Spectroscopic signatures and origin of hidden order in Ba_2MgReO_6

Received: 19 March 2024

Accepted: 24 October 2024

Published online: 29 November 2024

Check for updates

Jian-Rui Soh[1,2,8] ✉, Maximilian E. Merkel[3,8], Leonid V. Pourovskii[4,5], Ivica Živković[2], Oleg Malanyuk[2], Jana Pásztorová[2], Sonia Francoual[6], Daigorou Hirai[7], Andrea Urru[3], Davor Tolj[2], Dario Fiore Mosca[4,5], Oleg V. Yazyev[2], Nicola A. Spaldin[3], Claude Ederer[3] & Henrik M. Rønnow[2]

Clarifying the underlying mechanisms that govern ordering transitions in condensed matter systems is crucial for comprehending emergent properties and phenomena. While transitions are often classified as electronically driven or lattice-driven, we present a departure from this conventional picture in the case of the double perovskite Ba_2MgReO_6. Leveraging resonant and non-resonant elastic x-ray scattering techniques, we unveil the simultaneous ordering of structural distortions and charge quadrupoles at a critical temperature of $T_q \sim 33$ K. Using a variety of complementary first-principles-based computational techniques, we demonstrate that, while electronic interactions drive the ordering at T_q, it is ultimately the lattice distortions that dictate the specific ground state that emerges. Our findings highlight the crucial interplay between electronic and lattice degrees of freedom, providing a unified framework to understand and predict unconventional emergent phenomena in quantum materials.

Understanding symmetry-lowering phase transitions emerging from the ordering of electronic charge, orbital, magnetic, and/or structural degrees of freedom represents a fundamental objective of condensed matter physics. Recently, various materials containing 4*d* or 5*d* transition-metal cations have attracted considerable attention[1–15], owing to the comparable strengths of interactions that drive transitions. In particular, the size of the spin–orbit coupling, intersite electron hopping energies, and crystal-field effects in these materials are finely balanced, resulting in strongly entangled spin and orbital degrees of freedom that support exotic forms of order, such as higher-order magnetic or charge multipoles[16–19].

However, the direct detection of such multipolar order is challenging, and thus it is sometimes described as a "hidden" order. For example, the ordering of charge quadrupoles in several $5d^1$ and $5d^2$ double perovskite (DP) systems predicted by various theoretical studies[16,19–21] has eluded experimental verification thus far. Moreover, the emergence of multipolar order can be accompanied by structural distortions, which are generally easier to detect experimentally. In such cases, it is often unclear whether the initial driving force of the transition is purely electronic, and the structural distortion is merely a by-product of the electronic symmetry-lowering, or whether the structural distortion enables the transition in the first place. Furthermore, the boundaries between these categories are not always clear-cut, as numerous examples exhibit intricate phenomena stemming from the interplay between electronic and lattice interactions[22–26].

[1]Quantum Innovation Centre (Q.InC), Agency for Science Technology and Research (A*STAR), 2 Fusionopolis Way, Singapore 138634, Singapore. [2]Institute of Physics, École Polytechnique Fédérale de Lausanne (EPFL), CH-1015 Lausanne, Switzerland. [3]Materials Theory, ETH Zürich, Wolfgang-Pauli-Strasse 27, 8093 Zürich, Switzerland. [4]CPHT, CNRS, École polytechnique, Institut Polytechnique de Paris, 91120 Palaiseau, France. [5]Collège de France, Université PSL, 11 place Marcelin Berthelot, 75005 Paris, France. [6]Deutsches Elektronen-Synchrotron DESY, Notkestraße 85, 22607 Hamburg, Germany. [7]Department of Applied Physics, Nagoya University, Nagoya 464-8603, Japan. [8]These authors contributed equally: Jian-Rui Soh, Maximilian E. Merkel.
✉e-mail: Soh_Jian_Rui@imre.a-star.edu.sg

As an example from the class of $5d^1$ DPs with their especially delicate interplay between electronic and lattice degrees of freedom, here we study Ba_2MgReO_6 (hereafter BMRO) with a combination of advanced theoretical and experimental techniques. BMRO features Re cations on a face-centered cubic (fcc) lattice in a formally $5d^1$ electron configuration that is both strongly spin–orbit entangled and Jahn–Teller active due to its four-fold degenerate $J_{\text{eff}} = 3/2$ ground state[18].

First, using resonant and non-resonant elastic x-ray scattering, we present direct experimental evidence for the simultaneous long-range order of Re $5d^1$ electric quadrupoles ($q_\theta^{\mathbf{k}}$) and structural distortions of the ReO_6 octahedra ($d_\theta^{\mathbf{k}}$) below $T_q \approx 33$ K. Specifically, the $\theta = x^2-y^2$ mode exhibits an antiferroic arrangement with a propagation vector $\mathbf{k} = [001]$, while the $\theta = z^2$ mode displays ferroic $\mathbf{k} = [000]$ order (Fig. 1a, b, d, e). Crucially, the detection of the concomitant onset of the $q_{x^2-y^2}^{[001]}$ and $q_{z^2}^{[000]}$ quadrupolar orders alongside the $d_{x^2-y^2}^{[001]}$ and $d_{z^2}^{[000]}$ structural distortions in BMRO represents a clear experimental verification of several theoretical studies[3,19–21].

Second, we show that calculations where the role of the lattice distortions is neglected predict two competing quadrupolar orders, namely the antiferroic $q_{x^2-y^2}^{[001]}$ order of the experimental ground state and a ferroic $q_{xy}^{[000]}$ order, which was not detected in the experiment. Both types of quadrupolar orders are stabilized by intersite electronic interactions alone. Coupling with lattice deformations then lowers the relative energy of the $q_{x^2-y^2}^{[001]}$ to the extent that it forms the ground state, in agreement with the experimental findings.

This departure from the conventional role of the lattice as a stabilizer of orders that are already favored electronically underscores the necessity for a more nuanced understanding of ordering transitions, where the cooperative contributions of electronic interactions and structural distortions shape the emergent properties of quantum materials. By elucidating the intricate interplay between these degrees of freedom, our work sheds light on the nature of the cooperative behavior of instabilities in complex materials and paves the way for new insights regarding emergent phenomena.

Results

Prior experimental studies have reported two consecutive anomalies in the heat capacity of BMRO at temperatures $T_q = 33$ K and $T_m = 18$ K, demarcating three distinct phases[1–3]: (i) above T_q, in the paramagnetic-cubic phase, BMRO exhibits $Fm\bar{3}m$ symmetry with ReO_6 octahedra arranged on an fcc lattice; (ii) at T_q, a cubic-to-tetragonal structural distortion occurs, leading to a transition into the paramagnetic-tetragonal phase with $P4_2/mnm$ space group symmetry; (iii) below T_m, BMRO further develops long-ranged magnetic order and enters the magnetic-tetragonal phase.

Although theoretical predictions have suggested the simultaneous onset of structural distortion and charge quadrupolar order in BMRO below T_q[16,19–21], direct experimental evidence of quadrupolar order has not been demonstrated. Indeed, the preliminary x-ray scattering measurements of BMRO reported by Hirai et al.[3] focused only on the magnetic and structural order. In this work, we extend the resonant elastic x-ray scattering (REXS) approach and detect an additional

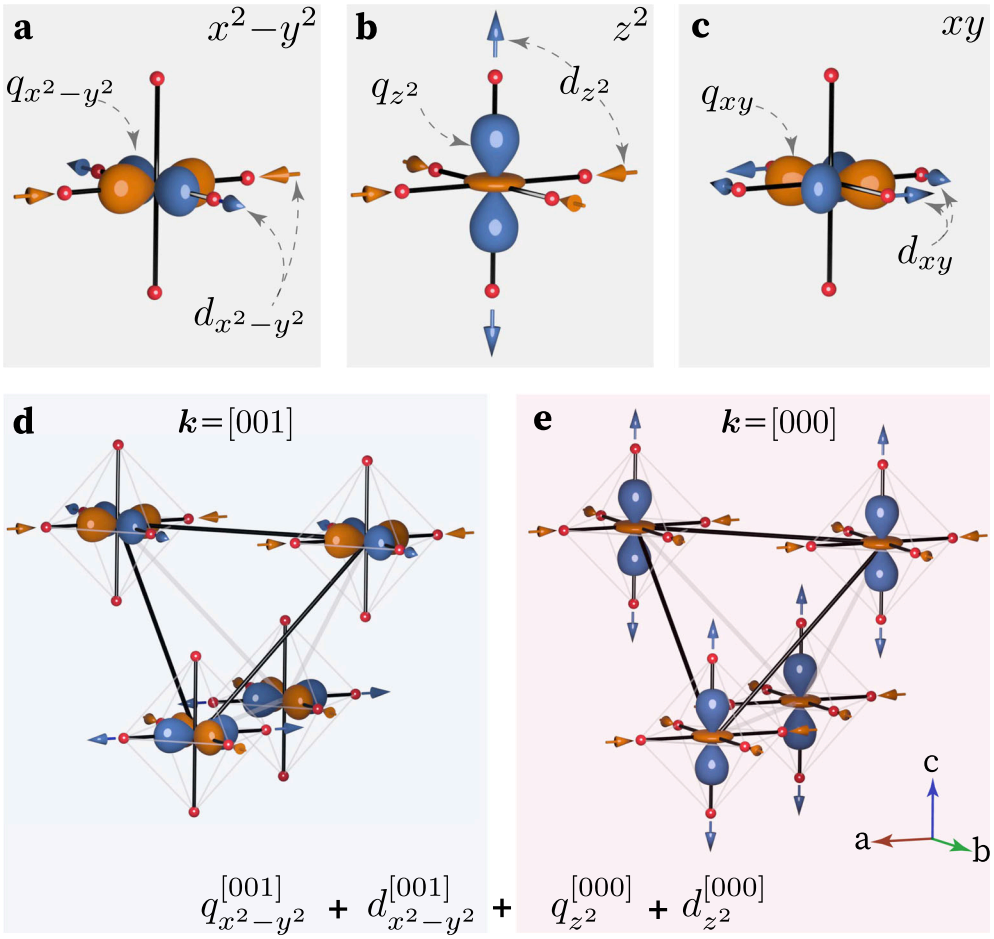

Fig. 1 | Lattice and electric-quadrupolar coupling and ordering. a–c The lattice deformations (d_θ) and charge quadrupoles (q_θ) with symmetry $\theta = x^2-y^2$, z^2 and xy, respectively. The blue and orange lobes of q_θ correspond to regions with excess and reduced electronic charge, respectively. **d**, **e** Below T_q, BMRO develops a simultaneous long-range order of the local distortion $d_\theta^{\mathbf{k}}$ and electric quadrupoles $q_\theta^{\mathbf{k}}$. **d** The $\theta = x^2-y^2$ component exhibits an antiferroic order with a $\mathbf{k} = [001]$ propagation vector. **e** The $\theta = z^2$ component displays ferroic, $\mathbf{k} = [000]$ arrangement.

https://doi.org/10.1038/s41467-024-53893-z

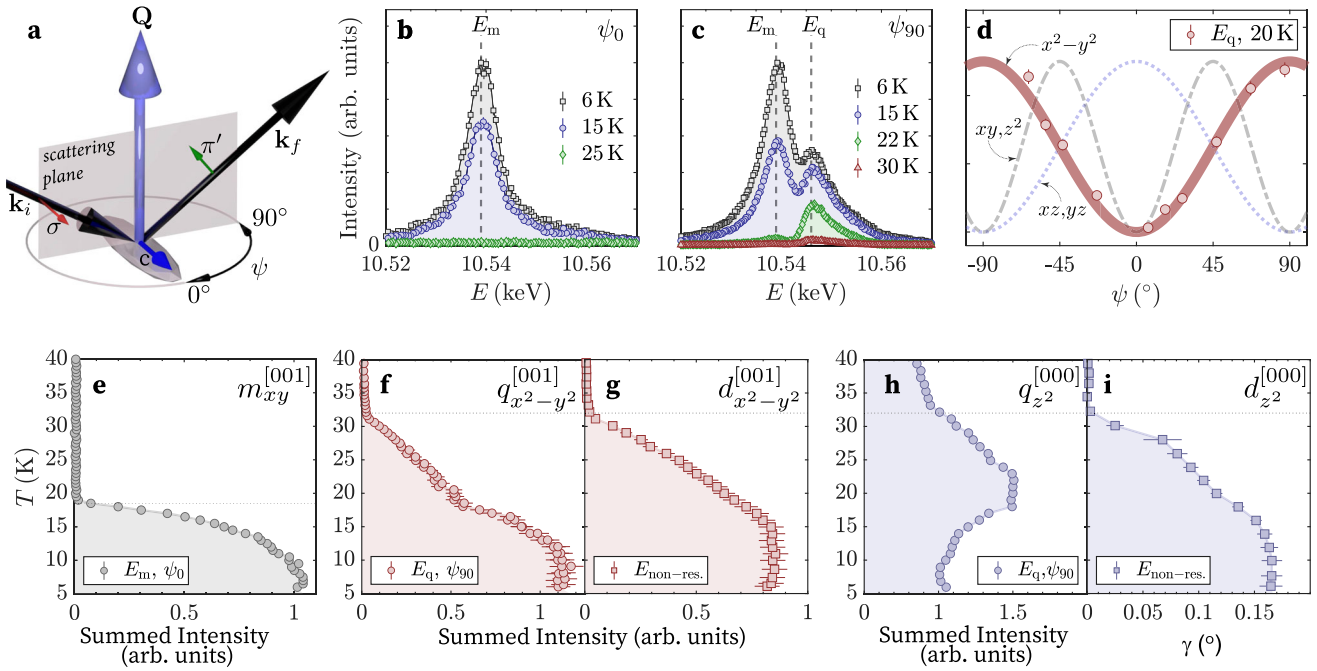

Fig. 2 | Direct detection of the charge quadrupolar, structural and magnetic order parameters in BMRO. a REXS experimental setup in the $\sigma \rightarrow \pi'$ scattering channel. The ψ_0 (ψ_{90}) orientation corresponds to the configuration where the crystal *c* axis points perpendicular (within) the vertical scattering plane. **b**, **c** Energy dependence of the **Q** = (5, 5, 0) Bragg reflection with the ψ_0 and ψ_{90} crystal orientations, at various temperatures. **d** Azimuthal dependence of the (5, 5, 0) reflection at E_q and at 20 K demonstrates the $\theta = x^2-y^2$ symmetry of the antiferroic quadrupolar $q_\theta^{[001]}$ order. The dashed (dotted) lines depict the calculated azimuthal dependence of the quadrupoles with xy,z^2 (xz,yz) symmetry. **e** Integrated intensity of the (5, 5, 0) peak at the magnetic resonance E_m and ψ_0 azimuth indicates the onset of the antiferroic $m_{xy}^{[001]}$ order of Re magnetic dipoles below 18 K. **f**, **g** Integrated intensity of the (5, 5, 0) and (5, 3, 0) peaks measured at E_q and off-resonance, respectively, to detect the antiferroic $q_{x^2-y^2}^{[001]}$ and $d_{x^2-y^2}^{[001]}$ orders. **h** The (10, 0, 0) peak measured at E_q resonance which is indicative of the ferroic $q_{z^2}^{[000]}$ order. **i** The γ splitting of the (10,0,0) reflection to reflect the ordering of $d_{z^2}^{[000]}$. The error bars correspond to the standard deviation.

resonance at E_q (~10.541 keV) that allows us to directly address the quadrupolar order developing at T_q.

Experimental results

Figure 2b, c displays the energy dependence of the **Q** = (5, 5, 0) Bragg reflection across the rhenium L_3 absorption edge for two different azimuthal angles, $\psi_0 = 0°$ and $\psi_{90} = 90°$, as illustrated in Fig. 2a. For the ψ_0 orientation at low temperatures ($T = 6$ K), we observe a single resonant peak centered at E_m (~10.535 keV), which is consistent with an earlier REXS study[3]. On the other hand, the ψ_{90} orientation reveals an additional resonance at E_q, which has not been reported before. The energy scans performed at elevated temperatures in both configurations demonstrate distinct behaviors: the peak at E_m disappears upon heating above T_m, whereas the peak at E_q persists well into the paramagnetic-tetragonal phase and vanishes at T_q.

To gain a deeper understanding of the origins of the two resonances, we examine the temperature dependence of the (5, 5, 0) reflection with the incident photon energy fixed at E_q and E_m, as shown in Fig. 2f, e, respectively. The resonant peak at E_m displays a temperature dependence characteristic of an order parameter below T_m, consistent with the anomaly observed in the magnetic susceptibility of BMRO[2]. Thus, we attribute the resonance at E_m to the antiferromagnetic **k** = [001] magnetic order of the Re sublattice, in line with the interpretation from the previously reported REXS study[3].

In contrast, the intensity of the (5, 5, 0) peak at the E_q resonance already exhibits a sharp increase below T_q, while BMRO remains in the paramagnetic phase [Fig. 2f]. As time-reversal symmetry is preserved, the observed REXS intensity originates[20] from the anisotropic tensor scattering from the antiferroic **k** = [001] order of Re $5d^1$ charge quadrupoles. This non-zero intensity of the (5, 5, 0) Bragg peak at E_q within the temperature range between T_m and T_q provides direct evidence for the long-range order of charge quadrupoles in the $5d^1$ double perovskite BMRO.

Charge quadrupoles can exhibit five different symmetry projections, $q_{x^2-y^2}$, q_{z^2}, q_{xy}, q_{xz} and q_{yz}. To distinguish between various contributions, we analyze the azimuthal dependence of the (5, 5, 0) Bragg peak at E_q in the paramagnetic tetragonal phase ($T = 25$ K), as shown in Fig. 2d. The data provides a consistent fit with antiferroic ordering of charge quadrupoles possessing x^2-y^2 symmetry, namely $q_{x^2-y^2}^{[001]}$. As shown by broken lines in Fig. 2d, our analysis clearly excludes the appearance of quadrupolar order with other symmetries ($\theta = z^2$, xy, xz, or yz).

Furthermore, the emergence of the $q_{x^2-y^2}^{[001]}$ quadrupolar order below T_q occurs concomitantly with the onset of the $d_{x^2-y^2}^{[001]}$ structural distortion, as shown by the temperature dependence of the (5, 3, 0) reflection measured at $E_{non\text{-}res.}$ (10.500 keV) (Fig. 2g). This structural peak, which is otherwise forbidden by the $Fm\bar{3}m$ cubic structure, arises from an antiferroic **k** = [001] ordering of x^2-y^2 distortions of the ReO_6 octahedron, as illustrated in Fig. 1d.

In addition to the antiferroic $q_{x^2-y^2}^{[001]}$ and $d_{x^2-y^2}^{[001]}$ orders, we also found evidence for the spontaneous ferroic **k** = [000] long-range ordering of z^2-type lattice distortion and charge quadrupoles below T_q (Fig. 1e). The former, $d_{z^2}^{[000]}$, manifests as a cubic-to-tetragonal structural distortion (Fig. 1e) as shown by the splitting of the (10, 0, 0) structural peak in Fig. 2i. On the other hand, discerning the experimental signature of the latter is more challenging as the scattered intensity from the $q_{z^2}^{[000]}$ order occurs at the same reciprocal space location as the structural peaks. To maximize the ferroquadrupolar signal, we use incident x-ray energy at E_q to benefit from REXS, in conjunction with scattering in the $\sigma \rightarrow \pi'$ channel (Fig. 2a) to suppress the signal from the structural peak. We are then able to observe a sharp increase in the scattering intensity just below T_q (Fig. 2h), indicative of

the onset of $q_{z^2}^{[000]}$ before the signal eventually decreases due to the splitting of the underlying structural peak (Supplementary Fig. 6).

Computational results

We now seek to understand the driving force behind the antiferroic x^2-y^2 and ferroic z^2 ordering (Fig. 1f, e) and its simultaneous onset in both the lattice and electronic degrees of freedom in the paramagnetic phase at T_q. To that end, we separate computationally the effect of the lattice instabilities of the ReO_6 octahedron from the intersite electronic interaction and investigate the resulting order parameters ($q_\theta^{\mathbf{k}}$, $d_\theta^{\mathbf{k}}$).

Through this comparison, we will demonstrate that (i) the local Jahn–Teller effect or (ii) the electronic effects separately cannot explain the experimentally observed orders. Only when (iii) both effects are accounted for can the ground state in BMRO be established. Hence, in the following sections, we examine these three scenarios.

We first investigate the role of the local Jahn–Teller effect by determining what kind of structural deformations (d_θ) have the propensity to lower the energy of BMRO. In order to go beyond isolated octahedral models[27,28], these distortions were applied to a ReO_6 octahedron embedded within the BMRO lattice. In this work, the potential energy landscape with respect to these distortion modes was determined by means of quantum-chemical (multi-reference configuration interaction) calculations.

Our calculations reveal a threefold degenerate global minima at −44 meV, which is established by e_g-type distortions alone (namely $d_{x^2-y^2}$ and d_{z^2} (Fig. 1a, b)). As shown in the energy landscape in Fig. 3a, these minima reside at $d_{z^2} = -0.060$ Å, along with their symmetry equivalents d_{x^2} and d_{y^2}. On the other hand, t_{2g}-type distortions alone (namely d_{xy} (Fig. 1c), d_{yz} and d_{xz}) can only lower the energy by 12 meV, at most, relative to the undistorted ReO_6 state and hence do not realize the ground state of the system.

Thus, the consideration of purely local effects alone can predict the same type of lattice distortions that were detected in the experiment, namely those of e_g symmetry. In particular, an alternating arrangement of $d_{x^2}<0$ and $d_{y^2}<0$ distortions, equivalent to $\pm(\sqrt{3}/2)d_{x^2-y^2} + (1/2)d_{z^2}$, is qualitatively consistent with the experimental distortion amplitudes[3], as indicated by the red dots in Fig. 3a. Nonetheless, a purely local model comprising a single ReO_6 octahedron is insufficient in predicting how the local distortions are arranged across the lattice, to form long-range order.

Next, to study the role of the electronic effects and determine what kind of long-range electronic order ($q_\theta^{\mathbf{k}}$) might arise, we calculate the intersite exchange interactions (IEI). To isolate the effect of the IEI from the local Jahn–Teller coupling, we consider the undistorted, cubic lattice of BMRO. The IEI is predicted to be the main ordering mechanism of many $5d^1$ and $5d^2$ DPs[16,17,19] and comes from the virtual hopping of the $5d$ electrons through ligands. In this work, they are calculated using the force theorem implemented within the Hubbard-I (FT-HI) framework[29].

The IEI can be written as couplings between local multipole operators $O_K^\theta(i)$[29,30] of order K and momentum projection θ at the Re site i. The multipole operators provide a complete representation of the electronic degrees of freedom in the Re-$J_{\text{eff}} = 3/2$ manifold, where $K = 1$, 2, and 3 label the dipole, quadrupole, and octupole moments, respectively. Our computed IEI for a given Re-Re bond $\langle ij \rangle$ can then be expressed as the matrix $V_{KK'}^{\theta\theta'}(ij)$, and the full IEI Hamiltonian reads

$$H_{\text{IEI}} = \sum_{\langle ij \rangle} \sum_{K\theta K'\theta'} V_{KK'}^{\theta\theta'}(ij) O_K^\theta(i) O_{K'}^{\theta'}(j), \tag{1}$$

where the first summation is over all nearest-neighbor Re–Re bonds (see the "Methods" section). The operators labeled with θ (θ') act on i (j) site, respectively.

The inset of Fig. 3b shows the calculated quadrupole–quadrupole IEI, which dominate over dipole and octupole terms, for a pair of Re atoms in the xy plane. While the interaction between the t_{2g} (xy, xz, yz) quadrupoles is negative, indicating the tendency towards a ferroic order, the strongest e_g (x^2-y^2, z^2) quadrupole coupling is positive and thus antiferroic. Thus, the ferroic t_{2g} order is expected to be favored over antiferroic orders, due to the geometrical frustration of the fcc lattice.

Based on these IEI, we identify the stable electronic orderings $q_\theta^{\mathbf{k}}$ by numerically solving Eq. (1) within the mean-field approximation. The resulting total energy as a function of the temperature is shown in Fig. 3b. A ferro $q_{xy}^{[000]}$ quadrupolar ordered state emerges with the highest ordering temperature $T_q = 68$ K. The competing phase is identified by solving Eq. (1) with the IEI between t_{2g} quadrupoles suppressed. In this case, the experimentally observed antiferroic $q_{x^2-y^2}^{[001]}$ order emerges at a slightly lower $T_q = 53$ K, indicating that the antiferroic e_g order is less stable than the ferroic t_{2g} quadrupolar order in this purely electronic model. Our mean-field calculations with the FT-HI-derived IEI overestimate the transition temperature T_q, which is expected due to the mean-field approximation and is in line with previous studies of DPs[31,32].

We complement these results on the electronic order with density-functional theory plus dynamical mean-field theory

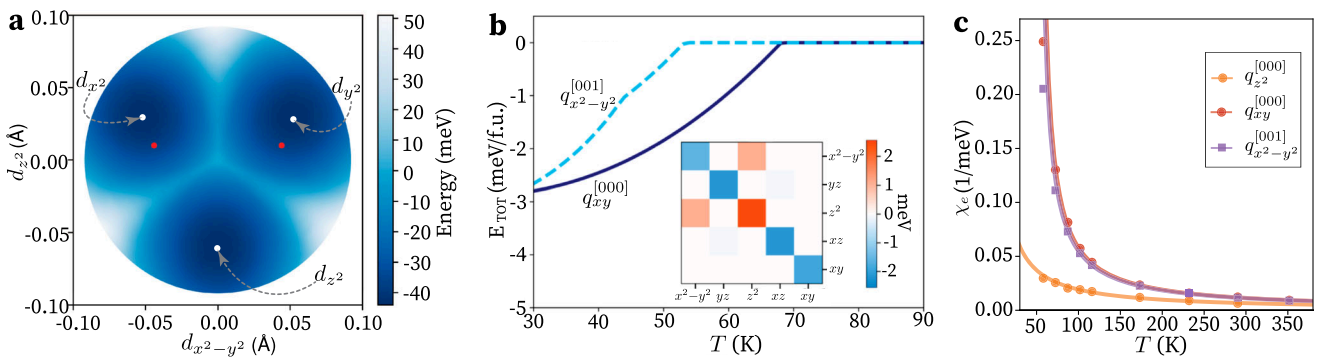

Fig. 3 | Calculations of BMRO. a The potential energy surface of a single ReO_6 octahedron in BMRO as a function of $d_{x^2-y^2}$ and d_{z^2} distortions, compared to the experimental octahedral distortions (denoted with the red dots)[3]. **b** Total energy E_{TOT} versus the temperature T calculated within the mean-field approximation from the ab-initio IEI Hamiltonian (Eq. (1)). The solid and dashed curves are the total energies of the t_{2g} ferro-$q_{xy}^{[000]}$ and e_g antiferro-$q_{x^2-y^2}^{[001]}$ orders, respectively. Inset: the quadrupole-quadrupole block of the IEI matrix V for the nearest-neighbor xy Re–Re bond, blue (red) colors correspond to ferro (antiferro) couplings. **c** The electronic susceptibility χ_e over the temperature T associated with the ferro xy and antiferroic $\mathbf{k} = [001]$ x^2-y^2 quadrupolar orders display Curie-Weiss behavior with a $T_q \sim 50$ K. On the other hand, the z^2 quadrupoles do not diverge at a temperature above zero and thus do not ferroically order spontaneously.

(DFT+DMFT) calculations that go beyond the quasi-atomic Hubbard-I approximation, again for the cubic, paramagnetic phase without lattice distortions. We compute the electronic susceptibilities $\chi_e(T)$ of cubic BMRO under small (anti-)ferroic quadrupolar fields[33] as a function of the temperature T, which are then fitted with a Curie–Weiss law, $\chi_e(T) \propto (T - T_q)^{-1}$.

As shown in Fig. 3c, χ_e diverges for both the $q_{xy}^{[000]}$ and $q_{x^2-y^2}^{[001]}$ orders. Consistent with the FT-HI results, this indicates the emergence of electronic quadrupolar long-range order at around 50K, with a slightly higher T_q for $q_{xy}^{[000]}$. The $q_{z^2}^{[000]}$ order, which also appeared in our REXS measurements, does not exhibit a divergence for $T > 0$, which indicates its inability to spontaneously order.

Together, the FT-HI and DFT+DMFT calculations with the lattice frozen to its high-symmetry structure draw a consistent picture, demonstrating that electronic interactions alone can stabilize long-range quadrupolar order. However, both calculations (where the role of the Jahn–Teller effect is neglected) indicate a slightly stronger tendency towards spontaneous ferro $q_{xy}^{[000]}$ quadrupolar order, contrary to the experimentally observed $q_{x^2-y^2}^{[001]}$ order.

Moreover, these predictions are inconsistent with the case when only local Jahn–Teller effects are considered as discussed in the previous section, where $d_{x^2-y^2}$ and d_{z^2} local distortions are preferred over d_{xy}. This contradiction clearly indicates that models that only consider the effects of IEI or local Jahn–Teller coupling separately are insufficient to comprehensively describe the emerging long-range order in BMRO.

Hence, we now combine the Jahn–Teller and electronic effects discussed before within a single computational framework. This is achieved by coupling the $q_{x^2-y^2}^{[001]}$, $q_{xy}^{[000]}$, and $q_{z^2}^{[000]}$ quadrupolar orderings to the $d_{x^2-y^2}^{[001]}$, $d_{xy}^{[000]}$, and $d_{z^2}^{[000]}$ distortion modes, respectively. For the two $\mathbf{k} = [000]$ modes, both homogeneous strain and internal oxygen displacements distort the ReO_6 octahedra in the same way, which we account for by defining the corresponding distortion amplitudes as two-component vectors $\mathbf{d}_\theta^{\mathbf{k}}$.

The leading order contribution of the structural deformation modes to the Landau-type free energy can be described as

$$F_{\mathrm{latt}}(q_\theta^{\mathbf{k}}, \mathbf{d}_\theta^{\mathbf{k}}) = -\frac{1}{2}\mathbf{g}_\theta^{\mathbf{k}} \cdot \mathbf{d}_\theta^{\mathbf{k}} q_\theta^{\mathbf{k}} + \frac{1}{2}\mathbf{d}_\theta^{\mathbf{k}} \cdot (\mathbf{K}_\theta^{\mathbf{k}} \mathbf{d}_\theta^{\mathbf{k}}), \tag{2}$$

where $\mathbf{g}_\theta^{\mathbf{k}}$ defines the bilinear coupling strength between the distortion $\mathbf{d}_\theta^{\mathbf{k}}$ and the quadrupole $q_\theta^{\mathbf{k}}$ of the same symmetry and the matrix $\mathbf{K}_\theta^{\mathbf{k}}$ parametrizes the energy cost for elastic lattice deformations[22,23,34]. A consequence of the bilinear electron-lattice coupling is that the quadrupole moments directly couple to distortions with

$$\mathbf{d}_\theta^{\mathbf{k}} = \frac{1}{2}(\mathbf{K}_\theta^{\mathbf{k}})^{-1} \cdot \mathbf{g}_\theta^{\mathbf{k}} q_\theta^{\mathbf{k}}, \tag{3}$$

which follows from minimizing the free energy with respect to $\mathbf{d}_\theta^{\mathbf{k}}$. This direct connection between the electronic and lattice degrees of freedom in Eq. (3) explains the simultaneous and proportional onset of their long-range ordering at T_q, as observed in our experiments (Fig. 2f–i).

At low temperatures, where the quadrupolar order is fully saturated ($|q_\theta^{\mathbf{k}}| = 1/2$), the free energy in Eq. (2) can be simplified to give $F_{\mathrm{latt}}^{\mathrm{sat}} = -\mathbf{g}_\theta^{\mathbf{k}} \cdot ((\mathbf{K}_\theta^{\mathbf{k}})^{-1} \mathbf{g}_\theta^{\mathbf{k}})/32$. Now, to ascertain which of the three types of order acquires the most stability, we compute the material constants $\mathbf{g}_\theta^{\mathbf{k}}$ and $\mathbf{K}_\theta^{\mathbf{k}}$ using DFT, so as to obtain the associated $F_{\mathrm{latt}}^{\mathrm{sat}}$ term (Table 1).

As shown in the last column of Table 1, the $F_{\mathrm{latt}}^{\mathrm{sat}}$ term stabilizes the experimentally observed $q_{x^2-y^2}^{[001]}$ order much more strongly compared to the $q_{xy}^{[000]}$ one, by a factor of 4. Crucially, when compared to the energy scales involved in Fig. 3b, the difference in $F_{\mathrm{latt}}^{\mathrm{sat}}$ between the two orderings is strong enough to change their relative stability, to the extent of establishing the $q_{x^2-y^2}^{[001]}$ order as the ground state, in accordance with the experimental findings. We note that the $F_{\mathrm{latt}}^{\mathrm{sat}}$ term also endows the $q_{z^2}^{[000]}$ order with additional stability, but is eventually not strong enough to compete with the $q_{x^2-y^2}^{[001]}$ order.

Our calculations demonstrate that, while charge quadrupolar order is energy lowering in the absence of lattice distortions, the electron-lattice coupling is crucial to favouring the experimentally observed order as the ground state, relative to other types of quadrupolar order.

In summary, our work provides direct experimental evidence of the elusive quadrupolar order 5*d* DPs, which has thus far remained hidden from conventional detection probes. We demonstrate that BMRO exhibits the simultaneous ordering of two distinct degrees of freedom: charge quadrupoles and local structural distortions. Theoretically, by treating these degrees of freedom equally, we demonstrate that the two orders work in tandem to collaboratively drive the phase transition. As such, our work underscores the necessity of a nuanced understanding of phase transitions, where distinct interactions contribute cooperatively, to shape the emergent properties of quantum materials.

Methods

Crystal growth and bulk characterization

The BMRO single crystals were synthesized via the flux growth method outlined in refs. 2,3. In this process, a mixture of BaO, MgO, and ReO_3 powders was combined with a flux comprising 36 wt% $BaCl_2$ and 64 wt % $MgCl_2$ within an argon-filled glove box. The resulting mixture was then sealed in a platinum tube and subjected to a gradual temperature increase up to 1300 °C. Subsequently, the tube was slowly cooled at a rate of 5 °C/h, reaching a final temperature of 900 °C. Once the system reached room temperature through natural cooling, the remaining flux was thoroughly eliminated by rinsing with distilled water. This process yielded octahedral-shaped BMRO single crystals with typical dimensions of approximately $1 \times 1 \times 1\,\mathrm{mm}^3$. The structure and quality of the obtained single crystals were verified using a laboratory 6-circle x-ray diffractometer (Rigaku).

Resonant elastic X-ray scattering

We performed low-temperature resonant elastic x-ray scattering (REXS) at the P09 beamline at PETRA III (DESY)[35] using a closed cycle cryostat. The crystal was aligned with the [110] axis in the vertical scattering plane, to study the (*h*,*h*,0) reflections in the specular diffraction condition. The angle ψ is defined as the rotation angle of the crystal about the scattering vector, **Q**. As such, the angle $\psi_0 = 0°$ ($\psi_{90} = 90°$) refers to the sample configuration in which the crystal [001] direction is perpendicular to (within) the vertical scattering plane. A pyrolytic graphite (002) analyzer crystal was used to discriminate between the σ' and π' scattered x-ray linear polarizations, which lie perpendicular and within the vertical scattering plane, respectively.

Quantum chemistry calculations

Embedding multi-reference quantum chemistry calculations were performed using the Molpro package[36]. The crystal structure for $Fm\bar{3}m$ configuration of BMRO was taken from ref. 3.

The quantum cluster under consideration consisted of 21 atoms: the ReO_6 octahedron with the 6 nearest Mg atoms and eight nearest Ba atoms. For the Re atom, core potentials and a basis set consisting of triple-zeta functions plus two polarization *f* functions were used[37]. All-electron triple-zeta functions were used for the surrounding O atoms[38]. Both Mg and Ba atoms in the cluster were described by an effective core potential and supplemented with a single *s* function[39,40]. The crystal lattice in which the cluster was embedded was constructed at

Table 1 | The lattice stabilization energy can be obtained from the electron-lattice coupling g and the elastic deformation K through a simple Landau free-energy expansion

k	θ	g (eV/Å)	K (eV/Å^2)	F^{sat}_{latt} (meV/f.u.)
[001]	x^2-y^2	2.52	19.9	−10.0
[000]	xy	$\begin{pmatrix}0.76\\0.92\end{pmatrix}$	$\begin{pmatrix}9.5 & 3.8\\3.8 & 21.8\end{pmatrix}$	−2.5
[000]	z^2	$\begin{pmatrix}1.93\\2.48\end{pmatrix}$	$\begin{pmatrix}18.4 & 13.1\\13.1 & 21.1\end{pmatrix}$	−9.6

the level of a Madelung ionic potential, with formal charges placed at the ionic sites. Beyond the first 500 ions, these formal charges were changed such that the unmodified direct sum potential matched the unmodified Ewald summation, as described in ref. 41.

For the complete active space self-consistent field (CASSCF) calculations, an active space of 5 orbitals ($3t_{2g}+2e_g$) was used. The optimization was carried out for an average of 5 states (ground state + 4 excited states) of the scalar relativistic Hamiltonian, with each state having a weight of one. Multi-reference configuration interaction (MRCI) treatment was performed with single and double substitutions with respect to the CASSCF reference, as described in refs. 42,43. Spin–orbit coupling was included as described in ref. 44.

The MRCI calculations were performed on the following grid: Isotropic distortions were varied from 0.5% to −1.5% with 0.5% steps. In this work, we show the results for an isotropic compression of 1%, for which the global energy minimum was found. For each value of isotropic distortion, a 60° sector of the d_{z^2}-$d_{x^2-y^2}$ plane was simulated, with the angle being varied with steps of 15° and radius being varied from 0% to 1.4%, with step of 0.1% (with % referencing the deviation of x-axis atoms from unperturbed 1.926 Å Re–O interatomic distance). The rest of the d_{z^2}-$d_{x^2-y^2}$ plane was filled, exploiting the symmetry of the $d_{x^2-y^2}$ amplitude and the 3-fold symmetry of the d_{z^2}-$d_{x^2-y^2}$ plane.

In the investigation of the t_{2g} modes, the isotropic and $d_{yz}+d_{xz}+d_{xy}$, as well as the d_{z^2} and $d_{x^2-y^2}$ deformation modes, were taken as orthogonal minimization axes to capture all (local) minima predicted by octahedral models[27,28]. Starting with the undistorted $Fm\bar{3}m$ structure, the search for minima was conducted by iterative optimization along these axes. Several minimization paths were considered that all converged back to the $d_{z^2}<0$ minimum mentioned in the "Results" section.

FT-HI calculations of exchange interactions

To calculate the IEI by the FT-HI method, we started with self-consistent DFT+DMFT calculations using the HI approximation to solve the Re 5d impurity problem. Our full-potential DFT+DMFT approach is based on the Wien2k DFT code[45] and TRIQS library implementation of DMFT[46,47]. In these calculations, we included spin–orbit coupling and used the experimental BMRO lattice structure, local-density approximation (LDA) exchange-correlation, 400 $\mathbf{k}$-points in the full Brillouin zone, as well as the Wien2k basis cutoff $R_{mt}K_{max}$=7. The projective Wannier orbitals[48,49] for Re t_{2g} orbitals are constructed from the corresponding manifold of t_{2g}-like bands. The rotationally invariant Kanamori interaction Hamiltonian was constructed using the parameters $U^K=3.77$ eV and $J^K_H=0.39$ eV; the corresponding interaction parameters for the full-5d shell are $U=F^0=3.2$ eV and $J_H=0.5$ eV in agreement with previous works[31,50]. After DFT+HI calculations were converged, the FT-HI method[29] was applied as post-processing on top of the converged DFT+HI electronic structure. We find, in agreement with previous calculations of IEI in 5d double perovskites[31,32,50], that due to a rapid decay of superexchange with the distance, only the nearest-neighbor IEI terms are important. We used the McPhase[51] package with an in-house module to solve the IEI Hamiltonian in the mean-field.

DFT+DMFT calculations

To calculate the quadrupolar susceptibility, we performed paramagnetic DFT+DMFT calculations, where the local impurity problem is solved using a numerically exact Quantum Monte Carlo method, which incorporates the hybridization with the effective bath. For the DFT calculations, we used VASP (version 6.4.1)[52,53] with the PBE PAW pseudopotentials[54] including the Ba-5s, Ba-5p, Mg-2p, and Re-5p semicore states as valence electrons. The calculations were performed in a 20-atom unit cell of the experimental, cubic $Fm\bar{3}m$ structure[3] with a $7\times7\times5$ reciprocal grid and a 600 eV plane-wave cutoff down to an energy convergence of 10^{-8} eV. We included spin-orbit coupling and constrain the magnetic moments to zero to enforce time-reversal symmetry. We generated Wannier orbitals from projections without localization with Wannier90 (version 3.1.0)[55] of the t_{2g}-like bands around the Fermi energy. The quadrupole operators O^θ_2 are upfolded from the $J_{eff}=3/2$ basis to this Wannier basis. We then ran one-shot DMFT calculations with solid_dmft (version 3.1.0)[56] (modified to implement the real spin–orbit-coupled basis $|xz\rangle, |-iyz\rangle, |ixy\rangle$ and the external field) using the CT-HYB Quantum-Monte-Carlo impurity solver[57], all from the TRIQS library[46,49]. We employed the same interaction parameters U^K and J^K_H as in FT-HI and time-reversal symmetrize the impurity Green's function from the solver to ensure a paramagnetic solution. The two Re sites in the unit cell were mapped onto each other by either the identity (for $q^{[000]}_{xy}$ and $q^{[000]}_{z^2}$) or a 90° rotation about the z-axis (for $q^{[001]}_{x^2-y^2}$) so that the two Re sites in the unit cell are symmetry equivalent. We applied an external field coupling to the different quadrupolar orders, which is defined as a local potential $\delta V=-s^{\mathbf{k}}_\theta O^\theta_2$[33], with a small $s^{\mathbf{k}}_\theta=1$ meV to ensure a linear, convergeable response. We then fitted the inverse susceptibility $(\chi^{\mathbf{k}}_\theta)^{-1}=s^{\mathbf{k}}_\theta/q^{\mathbf{k}}_\theta$ with a linear function according to the Curie–Weiss law. Below an electronic temperature of 50 K, the average sign from the impurity solver decays rapidly to zero and eventually makes convergence impossible.

Lattice-related constants

To extract the material constants $\mathbf{g}^{\mathbf{k}}_\theta$ and $\mathbf{K}^{\mathbf{k}}_\theta$, we applied small distortions $d^{[001]}_{x^2-y^2}$, $d^{[000]}_{xy}$, and $d^{[000]}_{z^2}$ with the same symmetry as the quadrupolar orders, or equivalently, X^+_2, Γ^+_5, and Γ^+_3 as defined in ISODISTORT[58,59]. We performed DFT calculations in the same setup as for the DFT+DMFT calculations, just without spin–orbit coupling, and get the total energy E_{DFT} as well as the matrices in orbital space of the local potential $\boldsymbol{\epsilon}$ and the local occupations $\boldsymbol{\rho}$ as a function of $\mathbf{d}^{\mathbf{k}}_\theta$. To calculate $\mathbf{K}^{\mathbf{k}}_\theta$, we followed refs. 22,34, extending the formalism to the multidimensional distortions and orbital-dependent quantities. We fitted the DFT energy for different mode amplitudes with a quadratic polynomial $E_{DFT}(\mathbf{d}^{\mathbf{k}}_\theta)=\mathbf{d}^{\mathbf{k}}_\theta\cdot(\mathbf{C}^{\mathbf{k}}_\theta\mathbf{d}^{\mathbf{k}}_\theta)/2$, where $\mathbf{C}^{\mathbf{k}}_\theta$ is a matrix. This energy is the sum of the mode stiffness energy $\mathbf{d}^{\mathbf{k}}_\theta\cdot(\mathbf{K}^{\mathbf{k}}_\theta\mathbf{d}^{\mathbf{k}}_\theta)/2$ from Eq. (2) and the DFT local occupation energy $\mathrm{Tr}(\boldsymbol{\rho}_{DFT}\boldsymbol{\epsilon})$[34]. If we take the derivative with respect to $\mathbf{d}^{\mathbf{k}}_\theta$ and use the Hellmann–Feynman theorem, we obtain

$$\mathbf{C}^{\mathbf{k}}_\theta\mathbf{d}^{\mathbf{k}}_\theta=\frac{\partial E_{DFT}}{\partial\mathbf{d}^{\mathbf{k}}_\theta}=\mathbf{K}^{\mathbf{k}}_\theta\mathbf{d}^{\mathbf{k}}_\theta+\sum_{mn}\rho_{mn}\frac{\partial\epsilon_{nm}}{\partial\mathbf{d}^{\mathbf{k}}_\theta},\tag{4}$$

and can, therefore, calculate $\mathbf{K}^{\mathbf{k}}_\theta$. $\mathbf{g}^{\mathbf{k}}_\theta$ directly from the local potential. If only the $J_{eff}=3/2$ quadruplet is occupied, as is the case in the DFT+DMFT calculations with spin–orbit coupling, we can rewrite $\mathrm{Tr}(\boldsymbol{\rho}\boldsymbol{\epsilon})=\mathrm{Tr}(\boldsymbol{\rho})\mathrm{Tr}(\boldsymbol{\epsilon})-\sum_\theta\mathrm{Tr}(-\boldsymbol{\epsilon}O^\theta_2)\mathrm{Tr}(\boldsymbol{\rho}O^\theta_2)$ for any time-reversal-symmetric occupation ρ. The first term is a mode-independent energy and the second term is the electron–lattice coupling that we can expand in leading order as $\mathrm{Tr}(-\boldsymbol{\epsilon}O^\theta_2)=\mathbf{g}^{\mathbf{k}}_\theta\cdot\mathbf{d}^{\mathbf{k}}_\theta/2$ so that the coupling strength in Eq. (2) is a linear fit to the multipole decomposition of $\boldsymbol{\epsilon}$ over $\mathbf{d}^{\mathbf{k}}_\theta$.

Data availability

The data from the REXS experiments, the DFT+DMFT calculations and the lattice-related constants presented in this study have been deposited in a Zenodo repository at https://doi.org/10.5281/zenodo.13831237.

References

1. Pásztorová, J., Tehrani, A. M., Živković, I., Spaldin, N. A. & Rønnow, H. M. Experimental and theoretical thermodynamic studies in Ba_2MgReO_6—the ground state in the context of Jahn–Teller effect. *J. Phys.: Condens. Matter* **35**, 245603 (2023).
2. Hirai, D. & Hiroi, Z. Successive symmetry breaking in a $J_{\rm eff}$ = 3/2 quartet in the spin–orbit coupled insulator Ba_2MgReO_6. *J. Phys. Soc. Jpn.* **88**, 064712 (2019).
3. Hirai, D. et al. Detection of multipolar orders in the spin–orbit-coupled 5*d* Mott insulator Ba_2MgReO_6. *Phys. Rev. Res.* **2**, 022063 (2020).
4. Erickson, A. S. et al. Ferromagnetism in the Mott insulator Ba_2NaOsO_6. *Phys. Rev. Lett.* **99**, 016404 (2007).
5. Lu, L. et al. Magnetism and local symmetry breaking in a Mott insulator with strong spin–orbit interactions. *Nat. Commun.* **8**, 14407 (2017).
6. Steele, A. J. et al. Low-moment magnetism in the double perovskites Ba_2MOsO_6 (*M* = Li, Na). *Phys. Rev. B* **84**, 144416 (2011).
7. Xu, L. et al. Covalency and vibronic couplings make a nonmagnetic *j* = 3/2 ion magnetic. *npj Quant. Mater.* **1**, 16029 (2016).
8. Mansouri Tehrani, A. et al. Charge multipole correlations and order in Cs_2TaCl_6. *Phys. Rev. Res.* **5**, L012010 (2023).
9. Ishikawa, H. et al. Phase transition in the $5d^1$ double perovskite Ba_2CaReO_6 induced by high magnetic field. *Phys. Rev. B* **104**, 174422 (2021).
10. Willa, K. et al. Phase transition preceding magnetic long-range order in the double perovskite Ba_2NaOsO_6. *Phys. Rev. B* **100**, 041108 (2019).
11. da Cruz Pinha Barbosa, V. et al. The impact of structural distortions on the magnetism of double perovskites containing $5d^1$ transition-metal ions. *Chem. Mater.* **34**, 1098–1109 (2022).
12. Marjerrison, C. A. et al. Cubic Re^{6+} ($5d^1$) double perovskites, Ba_2MgReO_6, Ba_2ZnReO_6, and $Ba_2Y_{2/3}ReO_6$: magnetism, heat capacity, μSR, and neutron scattering studies and comparison with theory. *Inorg. Chem.* **55**, 10701–10713 (2016).
13. Yamamura, K., Wakeshima, M. & Hinatsu, Y. Structural phase transition and magnetic properties of double perovskites Ba_2CaMO_6 (*M* = W, Re, Os). *J. Solid State Chem.* **179**, 605–612 (2006).
14. Ishikawa, H. et al. Ordering of hidden multipoles in spin-orbit entangled $5d^1$ Ta chlorides. *Phys. Rev. B* **100**, 045142 (2019).
15. Frontini, F. I. et al. Spin–orbit-lattice entangled state in A_2MgReO_6 (A = Ca, Sr, Ba) revealed by resonant inelastic x-ray scattering. *Phys. Rev. Lett.* **133**, 036501 (2024).
16. Chen, G., Pereira, R. & Balents, L. Exotic phases induced by strong spin–orbit coupling in ordered double perovskites. *Phys. Rev. B* **82**, 174440 (2010).
17. Chen, G. & Balents, L. Spin–orbit coupling in d^2 ordered double perovskites. *Phys. Rev. B* **84**, 094420 (2011).
18. Takayama, T., Chaloupka, J., Smerald, A., Khaliullin, G. & Takagi, H. Spin–orbit-entangled electronic phases in 4*d* and 5*d* transition-metal compounds. *J. Phys. Soc. Jpn.* **90**, 062001 (2021).
19. Svoboda, C., Zhang, W., Randeria, M. & Trivedi, N. Orbital order drives magnetic order in $5d^1$ and $5d^2$ double perovskite Mott insulators. *Phys. Rev. B* **104**, 024437 (2021).
20. Lovesey, S. W. & Khalyavin, D. D. Magnetic order and $5d^1$ multipoles in a rhenate double perovskite Ba_2MgReO_6. *Phys. Rev. B* **103**, 235160 (2021).
21. Iwahara, N. & Chibotaru, L. F. Vibronic order and emergent magnetism in cubic d^1 double perovskites. *Phys. Rev. B* **107**, L220404 (2023).
22. Peil, O. E., Hampel, A., Ederer, C. & Georges, A. Mechanism and control parameters of the coupled structural and metal–insulator transition in nickelates. *Phys. Rev. B* **99**, 245127 (2019).
23. Georgescu, A. B. & Millis, A. J. Quantifying the role of the lattice in metal–insulator phase transitions. *Commun. Phys.* **5**, 1–14 (2022).
24. Pavarini, E., Koch, E. & Lichtenstein, A. I. Mechanism for orbital ordering in $KCuF_3$. *Phys. Rev. Lett.* **101**, 266405 (2008).
25. Pavarini, E. & Koch, E. Origin of Jahn–Teller distortion and orbital order in $LaMnO_3$. *Phys. Rev. Lett.* **104**, 086402 (2010).
26. Zhang, X.-J., Koch, E. & Pavarini, E. $LaVO_3$: a true Kugel–Khomskii system. *Phys. Rev. B* **106**, 115110 (2022).
27. Bersuker, I. B. et al. (eds) *Vibronic Interactions in Molecules and Crystals*, Vol. 49 of *Springer Series in Chemical Physics* (Springer, Berlin, Heidelberg, 1989).
28. Streltsov, S. V., Temnikov, F. V., Kugel, K. I. & Khomskii, D. I. Interplay of the Jahn–Teller effect and spin-orbit coupling: the case of trigonal vibrations. *Phys. Rev. B* **105**, 205142 (2022).
29. Pourovskii, L. V. Two-site fluctuations and multipolar intersite exchange interactions in strongly correlated systems. *Phys. Rev. B* **94**, 115117 (2016).
30. Santini, P. et al. Multipolar interactions in *f*-electron systems: The paradigm of actinide dioxides. *Rev. Mod. Phys.* **81**, 807–863 (2009).
31. Pourovskii, L. V., Mosca, D. F. & Franchini, C. Ferro-octupolar order and low-energy excitations in d^2 double perovskites of osmium. *Phys. Rev. Lett.* **127**, 237201 (2021).
32. Pourovskii, L. V. Multipolar interactions and magnetic excitation gap in d^3 spin–orbit mott insulators. *Phys. Rev. B* **108**, 054436 (2023).
33. Schaufelberger, L., Merkel, M. E., Tehrani, A. M., Spaldin, N. A. & Ederer, C. Exploring energy landscapes of charge multipoles using constrained density functional theory. *Phys. Rev. Res.* **5**, 033172 (2023).
34. Georgescu, A. B., Peil, O. E., Disa, A. S., Georges, A. & Millis, A. J. Disentangling lattice and electronic contributions to the metal-insulator transition from bulk vs. layer confined $RNiO_3$. *Proc. Natl Acad. Sci. USA* **116**, 14434–14439 (2019).
35. Strempfer, J. et al. Resonant scattering and diffraction beamline P09 at PETRA III. *J. Synchrotron Radiat.* **20**, 541–549 (2013).
36. Werner, H.-J., Knowles, P., Knizia, G., Manby, F. & Schuetz, M. Molpro: a general-purpose quantum chemistry program package. *Wiley Interdiscip. Rev.: Comput. Mol. Sci.* **2**, 242–253 (2012).
37. Figgen, D., Peterson, K. A., Dolg, M. & Stoll, H. Energy-consistent pseudopotentials and correlation consistent basis sets for the 5*d* elements Hf–Pt. *J. Chem. Phys.* **130**, 164108 (2009).
38. Peterson, K. A. & Dunning Jr, T. H. Accurate correlation consistent basis sets for molecular core–valence correlation effects: the second row atoms Al–Ar, and the first row atoms B–Ne revisited. *J. Chem. Phys.* **117**, 10548–10560 (2002).
39. Fuentealba, P., von Szentpaly, L., Preuss, H. & Stoll, H. Pseudopotential calculations for alkaline-earth atoms. *J. Phys. B: At. Mol. Phys.* **18**, 1287 (1985).
40. Fuentealba, P.Unpublished (1998).
41. Klintenberg, M., Derenzo, S. & Weber, M. Accurate crystal fields for embedded cluster calculations. *Comput. Phys. Commun.* **131**, 120–128 (2000).
42. Knowles, P. J. & Werner, H.-J. Internally contracted multiconfiguration-reference configuration interaction calculations for excited states. *Theor. Chim. Acta* **84**, 95–103 (1992).
43. Werner, H. & Knowles, P. J. An efficient internally contracted multiconfiguration–reference configuration interaction method. *J. Chem. Phys.* **89**, 5803–5814 (1988).
44. Berning, A., Schweizer, M., Werner, H.-J., Knowles, P. J. & Palmieri, P. Spin–orbit matrix elements for internally contracted multireference configuration interaction wavefunctions. *Mol. Phys.* **98**, 1823–1833 (2000).

45. Blaha, P. et al. *WIEN2k, An augmented Plane Wave + Local Orbitals Program for Calculating Crystal Properties* (Karlheinz Schwarz, Technische Universität, Wien, Austria, 2018).
46. Parcollet, O. et al. TRIQS: a toolbox for research on interacting quantum systems. *Comput. Phys. Commun.* **196**, 398–415 (2015).
47. Aichhorn, M. et al. TRIQS/DFTTools: a TRIQS application for ab initio calculations of correlated materials. *Comput. Phys. Commun.* **204**, 200 – 208 (2016).
48. Amadon, B. et al. Plane-wave based electronic structure calculations for correlated materials using dynamical mean-field theory and projected local orbitals. *Phys. Rev. B* **77**, 205112 (2008).
49. Aichhorn, M. et al. Dynamical mean-field theory within an augmented plane-wave framework: assessing electronic correlations in the iron pnictide LaFeAsO. *Phys. Rev. B* **80**, 085101 (2009).
50. Fiore Mosca, D. et al. Interplay between multipolar spin interactions, Jahn-Teller effect, and electronic correlation in a $J_{\text{eff}} = \frac{3}{2}$ insulator. *Phys. Rev. B* **103**, 104401 (2021).
51. Rotter, M. Using McPhase to calculate magnetic phase diagrams of rare earth compounds. *J. Magn. Magn. Mater.* **272–276**(Suppl.), E481–E482 (2004).
52. Kresse, G. & Hafner, J. Ab initio molecular dynamics for liquid metals. *Phys. Rev. B* **47**, 558–561 (1993).
53. Kresse, G. & Furthmüller, J. Efficient iterative schemes for ab initio total-energy calculations using a plane-wave basis set. *Phys. Rev. B* **54**, 11169–11186 (1996).
54. Perdew, J. P., Burke, K. & Ernzerhof, M. Generalized gradient approximation made simple. *Phys. Rev. Lett.* **77**, 3865–3868 (1996).
55. Pizzi, G. et al. Wannier90 as a community code: new features and applications. *J. Phys.: Condens. Matter* **32**, 165902 (2020).
56. Merkel, M. E., Carta, A., Beck, S. & Hampel, A. solid_dmft: gray-boxing DFT+DMFT materials simulations with TRIQS. *J. Open Source Softw.* **7**, 4623 (2022).
57. Seth, P., Krivenko, I., Ferrero, M. & Parcollet, O. TRIQS/CTHYB: a continuous-time quantum Monte Carlo hybridisation expansion solver for quantum impurity problems. *Comput. Phys. Commun.* **200**, 274–284 (2016).
58. Campbell, B. J., Stokes, H. T., Tanner, D. E. & Hatch, D. M. ISODISPLACE: a web-based tool for exploring structural distortions. *J. Appl. Crystallogr.* **39**, 607–614 (2006).
59. Stokes, H. T., Hatch, D. M. & Campbell, B. J. *ISODISTORT, ISOTROPY Software Suite* https://iso.byu.edu (2022).

Acknowledgements

We thank Dan Porter, Chen Gang, Leon Balents, George Jackeli, Pablo J. Bereciartua Perez, Claude Monney, Yikai Yang, and Thorsten Schmitt for fruitful discussions, Sophie Beck for the implementation of the real formulation of spin–orbit coupling in DMFT in solid_dmft, and Christian Plueckthun for technical help. We acknowledge DESY (Hamburg, Germany), a member of the Helmholtz Association HGF, for the provision of experimental facilities. Beamtime was allocated for proposal I-20211583 EC. Quantum chemistry calculations were performed at the facilities of the Scientific IT and Application Support Center of EPFL. This work is supported by the ERC Synergy grant HERO under Grant # 810451 (J.-R.S., H.M.R., I.Z., N.A.S., A.U., J.P.), Swiss National Supercomputing Centre under project grant ID s1128 (M.E.M., C.E.), ETH Zürich (M.E.M., C.E., A.U., N.A.S.) and the Singapore National Science Scholarship from the Agency for Science Technology and Research (J.-R.S.). L.V.P. acknowledges the support of the computer team at CPHT.

Author contributions

J.-R.S. and H.M.R. designed the study. D.H. synthesized the single crystals. J.-R.S., J.P., D.H., I.Z., and D.T. characterized the single crystals. J.-R.S., J.P., S.F., I.Z., and D.T. performed the REXS experiments. M.E.M., L.V.P., O.M., A.U., N.A.S., O.V.Y., and D.F.M. carried out the theoretical calculations. J.-R.S., M.E.M., C.E., L.V.P., and O.M. wrote the manuscript with contributions from all authors.

Competing interests

The authors declare no competing interests.

Additional information

Supplementary information The online version contains supplementary material available at https://doi.org/10.1038/s41467-024-53893-z.

Correspondence and requests for materials should be addressed to Jian-Rui Soh.

Peer review information *Nature Communications* thanks the anonymous reviewer(s) for their contribution to the peer review of this work. A peer review file is available.